energies

MDPI

Article

Boosting the Transesterification Reaction by Adding a Single Na Atom into g-C_3N_4 Catalyst for Biodiesel Production: A First-Principles Study

Elim Kim [1,†], Ayuk Corlbert Ayuk [1,†], Deog-Keun Kim [2,*], Hak Joo Kim [3,*] and Hyung Chul Ham [1,*]

[1] Department of Chemistry and Chemical Engineering, Inha University, 100 Inha-ro, Michuhol-gu, Incheon 22212, Korea
[2] Energy Resources Upcycling Research Laboratory, Korea Institute of Energy Research, 152 Gajeong-ro, Yuseong-gu, Daejeon 34129, Korea
[3] Carbon Conversion Research Laboratory, Korea Institute of Energy Research, 152 Gajeong-ro, Yuseong-gu, Daejeon 34129, Korea
* Correspondence: dkkim@kier.re.kr (D.-K.K.); hakjukim@kier.re.kr (H.J.K.); ham.hyungchul@inha.ac.kr (H.C.H.)
† These authors contributed equally to this work.

Abstract: Increasing environmental problems and the energy crisis have led to interest in the development of alternative energy. One of the most promising sustainable alternatives to fossil fuel is biodiesel which is typically produced from the transesterification of refined vegetable oils using a homogeneous base catalyst. However, the current process limitations and steep production costs associated with the use of homogeneous catalysts have limited the global-wide acceptance of biodiesel. Heterogeneous catalysts have been considered suitable alternatives, but they still suffer from low catalytic activity. In this study, by using density functional theory (DFT) calculations, we examined the electronic and catalytic activity of the single Na-doped graphitic carbon nitrides (indicated by Na-doped g-C_3N_4) toward the efficient biodiesel (acetic acid methyl ester) production via the transesterification of triglyceride (triacetin). Our DFT calculation on reaction energetics and barriers revealed the enhancement of biodiesel productivity in the Na-doped catalyst compared to the pristine g-C_3N_4 catalyst. This was related to the large reduction of the barrier in the rate-limiting step. In addition, we investigated the acidity/basicity and electron distribution and density of state for the Na-doped and pristine g-C_3N_4 catalysts to better understand the role of the Na atom in determining the transesterification reaction. This study highlights the importance of the dopant in a g-C_3N_4 catalyst in determining the transesterification reaction, which may open new routes to improve biodiesel production.

Keywords: biodiesel; graphitic carbon nitrides; transesterification; heterogenous catalysts; methanol dissociation

Citation: Kim, E.; Ayuk, A.C.; Kim, D.-K.; Kim, H.J.; Ham, H.C. Boosting the Transesterification Reaction by Adding a Single Na Atom into g-C_3N_4 Catalyst for Biodiesel Production: A First-Principles Study. *Energies* **2022**, *15*, 8432. https://doi.org/10.3390/en15228432

Academic Editors: Hwachang Song and Hyun-Goo Kim

Received: 6 October 2022
Accepted: 9 November 2022
Published: 11 November 2022

1. Introduction

Increasing environmental problems and the energy crisis have led to the interest in the development of alternative energy. Biodiesel (derived from the transesterification reaction of triglycerides (bio-oil) with methanol on base catalyst) [1,2] is a promising alternative energy to replace fossil-based diesel fuel since it has many advantages such as renewability, nontoxicity, and low pollution emissions [3,4]. In industry, sodium hydroxide, potassium hydroxide, carbonates, or sodium methoxide are used as homogeneous base catalysts to produce biodiesel [5–8]. Although these catalysts show high efficiency and are inexpensive, they are limitedly applied to the biodiesel production process. Note that it is very difficult to separate and recover homogenous catalysts from biodiesel product, leading to a high process cost [4]. To solve these problems, heterogeneous catalysts for the transesterification reaction of bio-oil have been proposed, such as MgO/$MgAl_2O_4$,

CaO/SnO_2, KOH/ZSM5, Sr/MgO, KOH/NaX, and Fe_2O_3/CaO, which have displayed high activity toward the transesterification of triglycerides [9–17]. However, the leaching of some components of catalysts under excess methanol has been observed, leading to the reduction of catalytic efficiency. In recent years, magnetic nanoparticles such as Fe_3O_4-APEN [18], $MgFe_2O_4/CaO$ [19], and Fe_3O_4/SiO_2 [20] have emerged as catalysts for biodiesel production. Note that magnetic nanoparticles are easily recovered by magnetic support. However, these catalysts have drawbacks such as the growth of nanoparticles and a decrease in dispersibility in nanoparticles due to the loss of single domain by magnetic dipole attraction [21]. Thus, it is imperative to develop more efficient and sustainable catalysts for the commercialization of biodiesel production processes from waste oil.

Very recently, graphitic carbon nitrides (indicated by g-C_3N_4) were widely used as catalytic materials due to the low synthesis cost, and high stability [22–24], which have been applied to the hydrogen production [25–27], CO_2 reduction [28–31], and photocatalysts [32]. However, the g-C_3N_4 materials suffer from low catalytic activity. The doping of alkali metals into g-C_3N_4 has been accepted as one of methods to boost the reactivity [23,33].

This work aims to predict the electronic and catalytic activity of a single Na-doped g-C_3N_4 surface as a heterogeneous catalyst and to understand the mechanisms of biodiesel production with triacetin and methanol via the transesterification on g-C_3N_4 catalysts using spin-polarized density functional theory (DFT) calculations. This may open new routes to improve biodiesel production.

2. Computational Methods

In this work, all the first-principle calculations were performed based on the Kohn–Sham density functional theory (KS-DFT) as implemented in the Vienna Ab initio Simulation Package (VASP) [34,35]. The plane-wave basis sets with a kinetic energy cutoff of 400 eV were used to expand the valence electron wave functions [36]. The generalized gradient approximation within the Perdew–Burke–Ernzerhof (PBE) functional form was used as the exchange-correlation energy [37]. For all structural relaxations, the convergence criterion for the energy in electronic SCF iterations and the Hellmann–Feynman forces in ionic step iterations was set at 1.0×10^{-5} eV and -0.05 eV $Å^{-1}$. To reduce the interaction between neighboring layers, a large vacuum space of 15 Å was introduced along the z-axis. The Monkhorst–Pack special k-point mesh of $1 \times 1 \times 1$ was used to sample the first irreducible Brillouin zone. Furthermore, we analyzed the electronic structure properties that may give insight into the catalytic process of the reaction trajectories. In this regard, we predicted the energetic stability of the reactants and products by computing the adsorption energies (E_{ad}) in accordance with the equation

$$E_{ad} = E_{absorbent/substrate} - E_{absorbent} - E_{substrate} \quad (1)$$

where $E_{absorbent/substrate}$ stands for the total energy of the organic moieties adsorbed onto the g-C_3N_4 substrate. $E_{absorbent}$ is the total energy of the organic moieties during the different reaction steps, and $E_{substrate}$ corresponds to the total energy of the Na-doped g-C_3N_4 substrate, both inside the same unit cell. The reaction trajectories were computed using the string method [38,39] and the climbing images method [40] with a 0.05 eV of energy as a threshold force for both. For the barrier energy convergence criteria, we used six images from the reactants to the products. Charge transfer between the dopant and g-C_3N_4 substrate was also studied in accordance with the Bader charge analysis [41,42]. As is well known, the methodology is highly sensitive to the basis set used. Consequently, we were interested in providing qualitative trends into the electronic structure behavior of the organic moieties adsorbed on the doped g-C_3N_4 substrate. We also mapped the isosurfaces of the total charge density difference (defined as ρ_{diff} (r)) for the doped g-C_3N_4 catalysts. In this respect, ρ_{diff} (r) was plotted in the molecular viewer VESTA [43] according to

$$\rho_{diff}(r) = \rho_{dopant/substrate}(r) - \rho_{dopant}(r) - \rho_{substrate}(r) \quad (2)$$

where $\rho_{dopant/substrate}$ (r) refers to the charge density of the doped g-C_3N_4 system, ρ_{dopant} (r) is the charge density of the isolated dopant and $\rho_{substrate}$ (r) corresponds to the charge density of pristine g-C_3N_4 surface.

3. Results

3.1. Property of Na-Doped g-C_3N_4 Catalyst

A 3 × 3 supercell of g-C_3N_4 was used to design our model structure of Na-doped g-C_3N_4 consisting of 54 carbon atoms, 72 Nitrogen atoms, and 1 Sodium atom [44–46]. The optimized structure for Na-doped g-C_3N_4 is shown in Figure 1 above, with a lattice parameter of 21.42 Å. The C-N near the Na atom has a bond length of 1.33 Å, while the rest have a bond length of 1.4 Å. This agrees with previous theoretical results [47]. As for the Na-doped g-C_3N_4 model, the substitution model, namely replacing nonmetal C and N atoms by Na-atom, was not considered because nonmetal and metal are essentially different. The Na atom was placed at the triangular-like vacant site since it has adequate space to accommodate Na atoms with a relatively larger radius. The binding energy (referred to as E_b) of Na-doped g-C_3N_4, which was calculated by E (total energy of metal and C_3N_4 slab)–E (energy of C_3N_4 slab)–E (energy of a single Na atom) and was calculated to be −3.25 eV, indicating that it is thermodynamically stable.

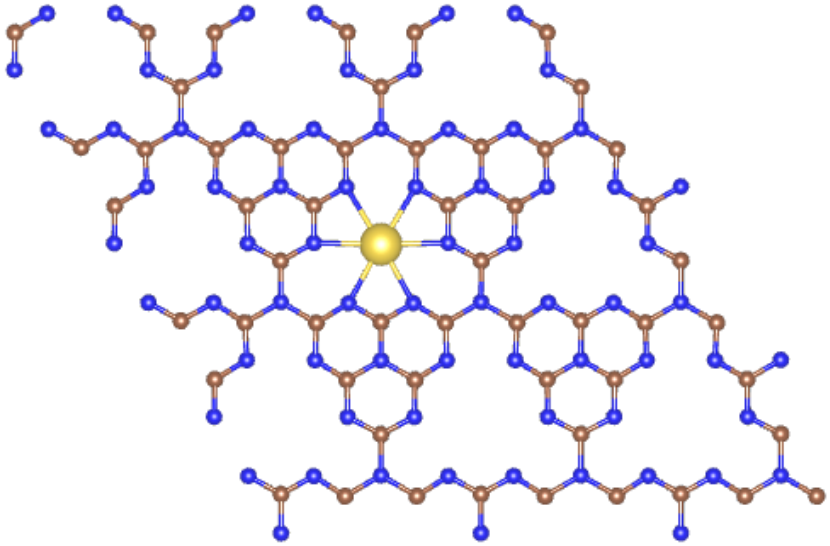

Figure 1. Optimized structure of Na-doped g-C_3N_4 catalyst. Blue, brown, and yellow balls indicate carbon, nitrogen, and sodium, respectively.

We performed the total density of state (DOS) calculation for the Na-doped and pristine C_3N_4 catalysts (see Figure 2) to gain more insight into the effect of Na dopant on the electronic structure of pristine C_3N_4. There was a slight change in the calculated bandgap (E_g) of pristine and Na-doped g-C_3N_4, with pristine having a GG-PBE functional calculated E_g of 0.655 eV, which is consistent with the reported value in [47]. In comparison, the E_g calculated by GGA-PBE functional for Na-doped was 0.545 eV. The reduction in the bandgap was consistent with Ma et al. report on bandgap reduction from 2.70 eV to 2.10 eV when g-C_3N_4 is doped with a sulfur atom [47]. This suggests that the Na-atom enhances the electronic property of the pristine g-C_3N_4, which may result in the improved catalytic activity of the Na-doped g-C_3N_4. In addition, as shown in Figure 2, the Femi level energy of the Na-doped g-C_3N_4 catalyst was located at the edge of the conduction band and the DOS at the Fermi level was increased. In contrast, in the pristine g-C_3N_4, the Femi level was at the edge of the valence band and the DOS at the Fermi level was almost zero; this further indicates that the Na-atom enhanced the electronic property of the g-C_3N_4.

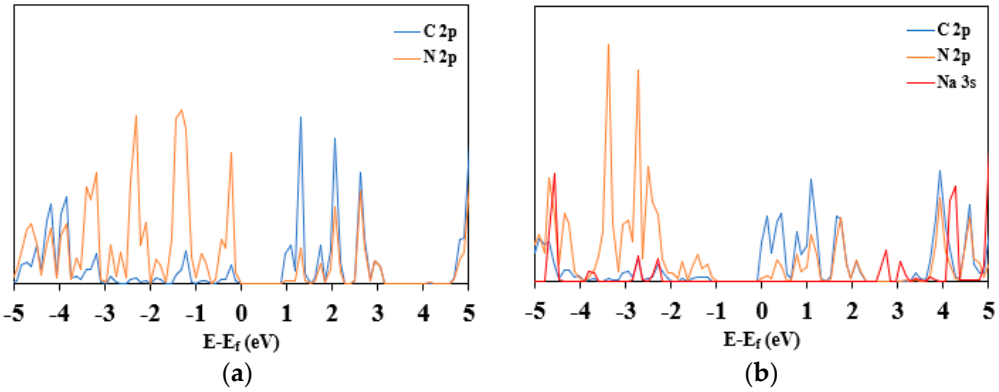

Figure 2. Electronic structure per atom for (**a**) pristine g-C_3N_4; (**b**) Na-doped g-C_3N_4.

To understand the charge transfer mechanism between the dopant (Na) and the g-C_3N_4, we performed the charge difference analysis as suggested by Equation (2). Such an equation was considered to plot the isosurfaces of the density difference. The yellow regions correspond to zones where the electronic charge was depleted, while the light blue region corresponds to zones where electronic charges were transferred. The ρ_{diff} (r) isosurface for the Na-doped g-C_3N_4 is shown in Figure 3. We find the charge loss of the Na and C (nearby Na) atom site and the charge gain of the N site. This indicates that the Na and C atom act as the active Lewis base site, while the N atom acts as the active Lewis acid site for Na-doped g-C_3N_4 because Na and C are an electron donor while N is an electron acceptor. In the case of pristine g-C_3N_4, we consider C and N sites as the active base and acid sites, respectively. For the Na-doped C_3N_4 catalyst, the geometric structure of Na-C and Na-N are considered as the adsorption site for our organic motifs. Furthermore, to evaluate the electron density rearrangement upon doping, we conducted a Bader charge analysis of pristine and Na-doped g-C_3N_4 systems. The change in effective atomic charges are shown in Table 1. The negative and positive values indicate the number of electrons gained or lost by each element in the system. We see that the N-atom gained electrons from the C and dopant atoms. By Bader charge analysis, we find that the C and N (nearby Na) sites of Na-doped g-C_3N_4 were more changed than the C and N sites of pristine g-C_3N_4 due to Na doping. Plus, the C site of Na-doped g-C_3N_4 lost more electrons than the Na site. This means that the C site was more active as the Lewis base site compared to the Na site.

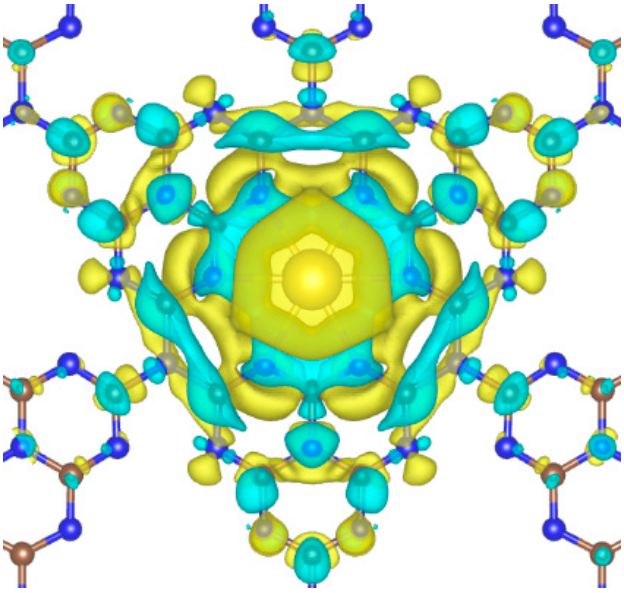

Figure 3. Charge density difference at the isosurface of -4.12×10^{-4} e/A and 4.12×10^{-4} e/A. Blue is electron gain, yellow is electron loss.

Table 1. Bader atomic charge change (indicated by ΔQ) of Na-doped g-C_3N_4 and pristine g-C_3N_4 with respect to the isolated atoms (each of ZVAL, N = 5, C = 4, Na = 1). It shows the C and each dopant loses some valence charge to the N atom, C and N are the local Bader charge near the Na atom.

Catalyst	C/ΔQ (e)	N/ΔQ (e)	Dopant/ΔQ (e)
Pristine	1.511	−1.127	N/A
Na-doped	1.532	−1.186	0.828

To better understand the catalytic activity of g-C_3N_4-based catalyst, we developed a method for predicting the acidity and basicity of our Na-doped g-C_3N_4 catalyst by calculating the CO_2 and NH_3 adsorption energies on the Na-doped g-C_3N_4 and pristine g-C_3N_4 catalysts (See Table 2). Here, the CO_2 adsorption energy indicates the degree of Lewis basicity (electron donor), while the NH_3 adsorption energy displays the Lewis acidity (electron acceptor). Our DFT calculation shows that the adsorption energies of CO_2 and NH_3 are −4.95 and −5.27 eV for Na-doped g-C_3N_4 and −5.12 and −5.23 eV for pristine g-C_3N_4, respectively (Note the strong adsorption of both molecules on the surface of catalysts as shown in Figure 4), implying that the Na site has a slightly higher Lewis acidity in the Na-doped g-C_3N_4 case than the pristine case, while for the Lewis basicity the opposite is true. This is related to the positive characteristics of the Na atom induced by the electronic charge loss of the Na atom to neighboring N atoms as mentioned in the previous section.

Table 2. Adsorption energies (E_{ad}) of carbon dioxide and ammonia with pristine g-C_3N_4 and Na-doped g-C_3N_4.Unit is given in eV.

Catalyst	E_{ad} [CO_2]	E_{ad} [NH_3]
Pristine	−5.12	−5.23
Na-doped	−4.95	−5.27

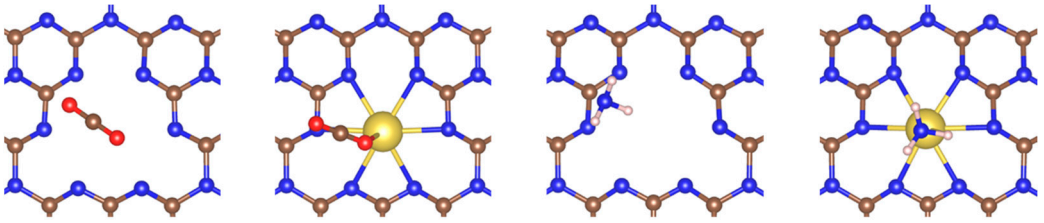

Figure 4. Optimized structure of (**a**) CO_2 adsorption on Pristine g-C_3N_4; (**b**) Na-doped g-C_3N_4; (**c**) NH_3 adsorption on Pristine g-C_3N_4; (**d**) Na-doped g-C_3N_4. Blue, brown, and yellow balls indicate carbon, nitrogen, and sodium, respectively.

3.2. Transesterification Mechanism of Triacetin on Catalysts

We examined the transesterification reaction of triacetin on the surface of Na-doped g-C_3N_4 and pristine g-C_3N_4 catalysts [48,49]. Here, we chose a triacetin molecule [$C_3H_5(OCOCH_3)_3$] for representing a triglyceride (bio-oil) [Figure 5a]. As shown in Figure 6, the first step for the transesterification reaction is the methanol (CH_3OH) adsorption on the catalyst surface [(1) CH_3OH (g) → CH_3OH*], which decomposes into the methoxy (CH_3O*) and H* by C—H bond dissociation [(2) CH_3OH* → CH_3O* + H*]. Then, triacetin (indicated by TA) is adsorbed on the catalyst [(3) $C_3H_5(OCOCH_3)_3$ → $C_3H_5(OCOCH_3)_3$*] and then is reacted by adsorbed CH_3O*, yielding the $C_3H_5(OCOCH_3)OCH_3$* compound (referred as TA-OCH_3) [(4) CH_3O* + $C_3H_5(OCOCH_3)_3$* → $C_3H_5(OCOCH_3)_3OCH_3$*]. Note that the O moiety of CH_3O is inserted into the C atom of the C=O group in $C_3H_5(OCOCH_3)_3$. Next, the biodiesel CH_3COOCH_3* [acetic acid methyl ester(denoted as AAME)] is produced by the C—O bond scission of $C_3H_5(OCOCH_3)_3OCH_3$* [(5) $C_3H_5(OCOCH_3)_3OCH_3$* → CH_3COOCH_3* +

$C_3H_5(OCOCH_3)_2O^*$] and is desorbed off [(6) $CH_3COOCH_3^* \rightarrow CH_3COOCH_3^*$ (g)]. Finally, $C_3H_5(OCOCH_3)_2O^*$ (displayed as DAO) undergoes the hydrogenation reaction, leading to diacetin [$C_3H_5(OCOCH_3)_2OH^*$] (indicated by DAOH) [(7) $C_3H_5(OCOCH_3)_2O^* + H^* \rightarrow C_3H_5(OCOCH_3)_2OH^*$].

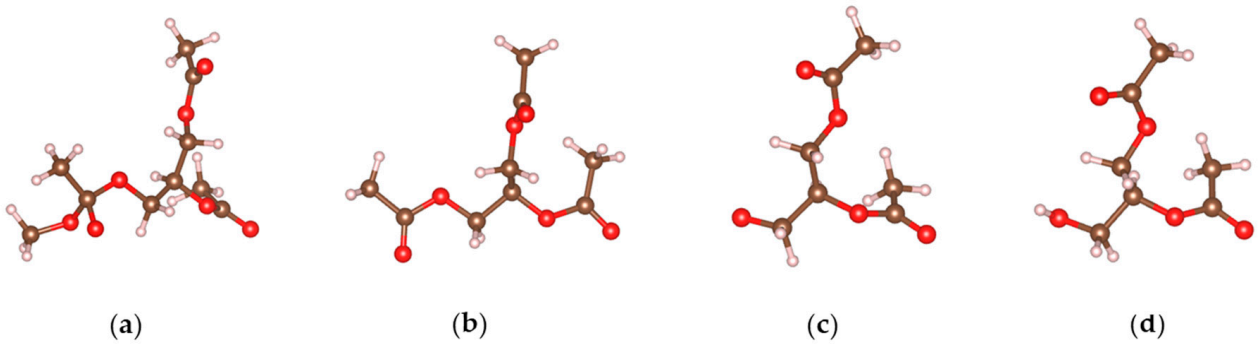

Figure 5. The structure of (**a**) triacetin [$C_3H_5(OCOCH_3)_3$] (TA), (**b**) $C_3H_5(OCOCH_3)OCH_3^*$ (TA-OCH_3) (**c**) DA–$C_3H_5(OCOCH_3)_2O^*$ (DAO) and (**d**) diacetin [$C_3H_5(OCOCH_3)_2OH^*$] (DAOH). Brown, white, and red balls indicate carbon, hydrogen, and oxygen atoms, respectively.

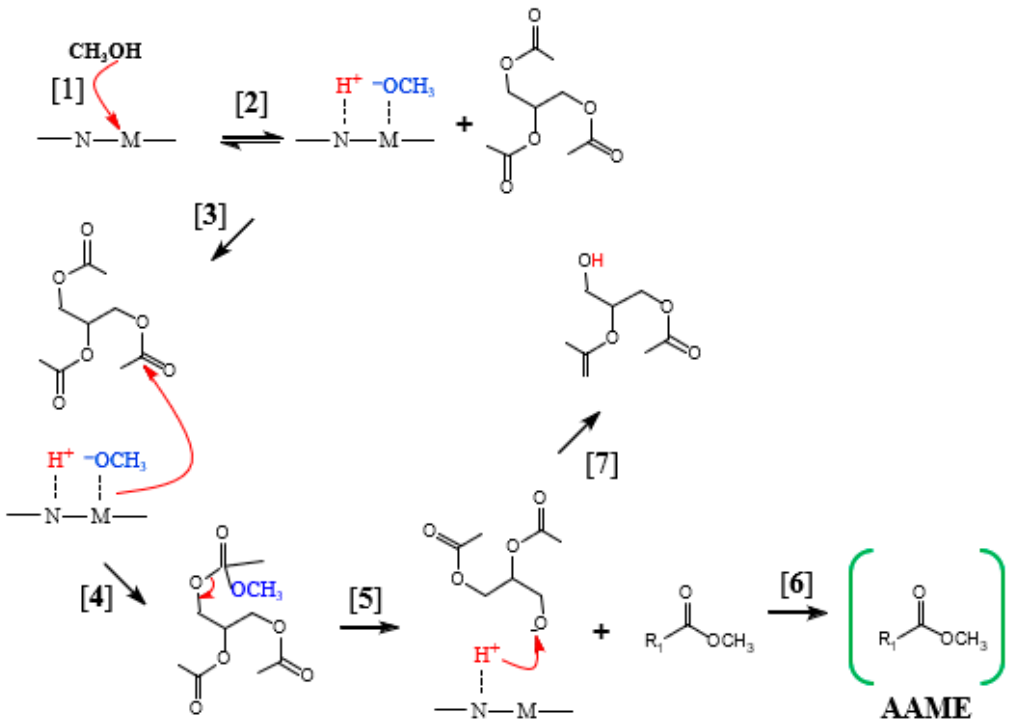

Figure 6. Reaction pathways of transesterification on the heterogenous catalysts.

3.3. CH_3OH Dissociation Reaction on Na-Doped g-C_3N_4 and Pristine g-C_3N_4

The reactivity of Na-doped g-C_3N_4 and pristine g-C_3N_4 catalyst toward the first stage of transesterification of triacetin (CH_3O and H formation via CH_3OH decomposition) can be the key reaction to produce biodiesel (acetic acid methyl ester, AAME) since the activity of formed CH_3O and H species on the catalyst surface play an important role in determining the subsequent reaction energetics and kinetics. Table 3 shows the adsorption energy (E_{ad}) of CH_3OH, CH_3O, H and the reaction energy (E_r) for the (1) $CH_3OH^* \rightarrow CH_3O^* + H^*$ step. We see the strong affinity of CH_3OH on both Na-doped g-C_3N_4 ($E_{ad} = -5.23$ eV) and pristine g-C_3N_4 ($E_{ad} = -5.30$ eV) catalysts. Next, our DFT calculation predicts that the reaction energy of Na-doped g-C_3N_4 ($E_r = -4.29$ eV) is more exothermic than the pristine g-C_3N_4 case ($E_r = -2.95$ eV), suggesting that the CH_3OH decomposition can occur more favorably in the Na-doped catalyst. This is related to the increase in adsorption strength

in CH_3O by 1.41 eV on the Na-doped g-C_3N_4 catalyst compared to the pristine g-C_3N_4 case. Here, the CH_3O adsorbs through its oxygen bonding with the dopant Na atom. Note that the O–Na bond distance in CH_3O adsorption is 1.50 Å and atomic H is bound to the N-atom where the N–H distances for Na system is 1.06 Å.

Table 3. Calculated adsorption energy (E_{ad}) of CH_3OH, CH_3O, H and reaction energy (E_r) of CH_3OH dissociation reaction on Na-doped g-C_3N_4 and pristine g-C_3N_4. Unit is given in eV.

Catalyst	CH_3OH	CH_3O	H	E_r
Pristine	−5.08	−5.24	−7.63	−3.17
Na	−5.23	−6.65	−7.50	−4.29

Figures 7 and 8 show the potential energy diagram (PED) and molecular configurations of the reactant, transition state (indicated by TS), and product for the $CH_3OH^* \rightarrow CH_3O^* + H^*$ reaction on the surface of pristine g-C_3N_4 and Na-doped g-C_3N_4 catalysts. Figure 8 shows the structure of the initial, transition, and final state of the $CH_3OH \rightarrow CH_3O + H$ reaction on catalysts. Here, the climbing image nudged elastic band (CI-NEB) method (which can determine the minimum energy path) is used to find the transition state and, in turn, the reaction barrier (denoted as E_{barr}). Our DFT calculation shows that the activation energy of the Na-doped g-C_3N_4 [E_{barr} = 1.53 eV] for the $CH_3OH \rightarrow CH_3O + H$ reaction is reduced compared to the pristine g-C_3N_4 system [E_{barr} = 1.69 eV]. This implies that the CH_3O—H bond scission occurs faster in the Na-doped g-C_3N_4 and, in turn, the yield of biodiesel production may be increased through the transesterification process.

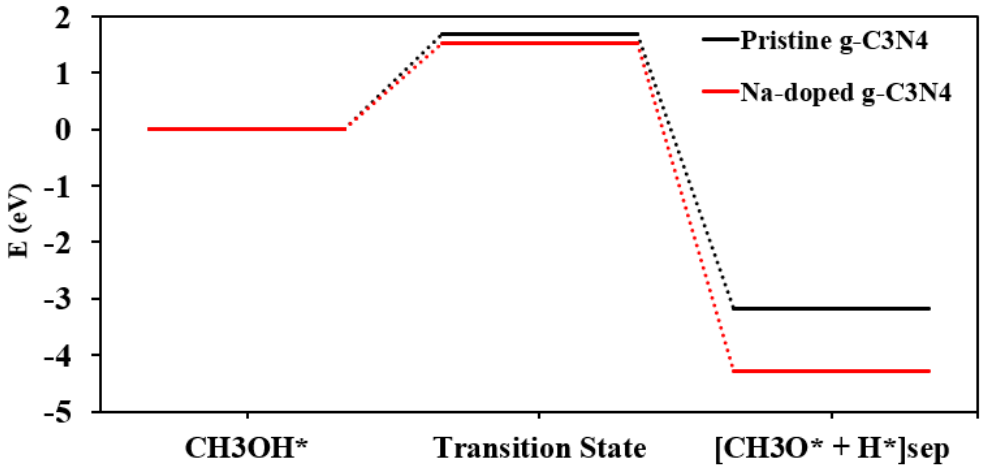

Figure 7. Potential energy diagram of Na-doped g-C_3N_4 and pristine g-C_3N_4 for methanol dissociation reaction.

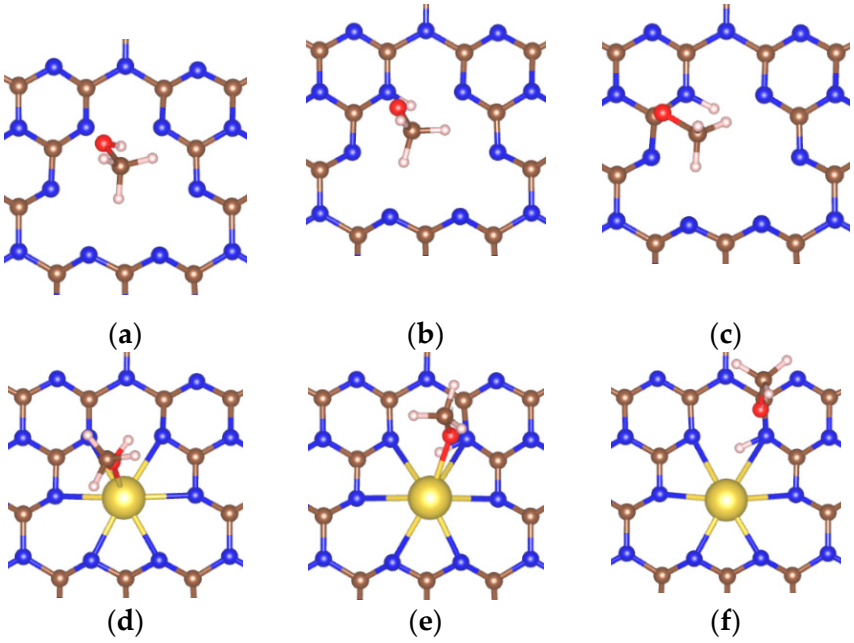

Figure 8. Structure of initial, transition, final state for $CH_3OH \rightarrow CH_3O^* + H^*$ on (**a**–**c**) pristine g-C_3N_4 and (**d**–**f**) Na-doped g-C_3N_4. Blue, brown, yellow, white, and red balls indicate nitrogen, carbon, sodium, hydrogen, and oxygen, respectively.

3.4. Biodiesel Production via Transesterification of Triacetin and Methoxy on Na-doped g-C_3N_4 and Pristine g-C_3N_4

Figures 9–11 show the potential energy diagram and intermediate structure for the transesterification of triacetin with CH_3O^* on catalyst surfaces. The reaction energy and barrier of each reaction is also shown in Table 4. First, the triacetin (TA) adsorption energy [(3) $C_3H_5(OCOCH_3)_3 \rightarrow C_3H_5(OCOCH_3)_3^*$] on the Na-doped g-$C_3N_4$ and pristine g-C_3N_4 surfaces is calculated to be −5.39 and −5.30 eV, respectively. Second, looking at the (4) $CH_3O^* + C_3H_5(OCOCH_3)_3^* \rightarrow C_3H_5(OCOCH_3)_3OCH_3^*$ reaction, the barrier for the Na-doped case is 0.94 eV, which is substantially higher than the pristine case [E_{barr} = 0.41 eV]. This is related to the large increase in stability (more exothermic proximity energy) in the co-adsorbed CH_3O^* and $C_3H_5(OCOCH_3)_3^*$ state for the Na-doped catalyst. Note that the proximity energy (which is defined as the energy required for the co-adsorbed state from the complete separation of CH_3O^* and $C_3H_5(OCOCH_3)_3^*$) for Na-doped case is highly exothermic by 1.56 eV compared to the pristine case. Next, for the production of AAME and DAO from TA-OCH_3 via the (5) $C_3H_5(OCOCH_3)_3OCH_3^*$ (TA-OCH_3) $\rightarrow CH_3COOCH_3^*$ (AAME) + $C_3H_5(OCOCH_3)_2O^*$ (DAO) reaction, the barrier in the Na-doped catalyst is predicted to be 0.43 eV, while for the pristine case, the reaction is the non-activated process (barrier-less reaction). Then, the biodiesel (AAME) is desorbed off the catalyst with the endothermic energy change of 0.19 (pristine) and 0.29 eV (Na-doped). Taking a look at the formation of diacetin (DAOH) by the hydrogenation via the (7) $C_3H_5(OCOCH_3)_2O^* + H^* \rightarrow C_3H_5(OCOCH_3)_2OH^*$ reaction, the activation barrier for Na-doped catalyst is reduced by 0.20 eV compared to the pristine case.

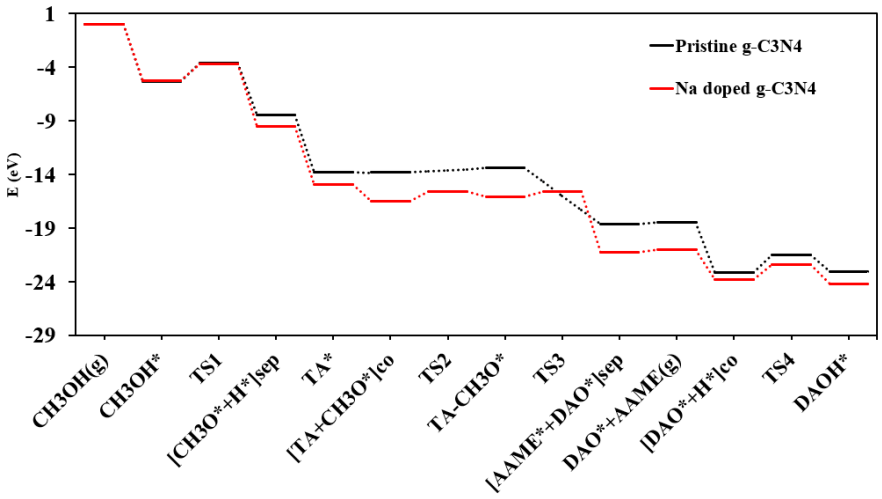

Figure 9. Potential energy diagram for the transesterification of tri-acetin with CH_3OH on catalyst surfaces on the Na-doped and pristine g-C_3N_4 catalyst. Here, the TS, TA, AAME, DAOH, DAO, and TA-OCH_3 indicate the transition state, triacetin [$C_3H_5(OCOCH_3)_3$], acetic acid methyl ester [CH_3COOCH_3], diacetin [$C_3H_5(OCOCH_3)_2OH$], $C_3H_5(OCOCH_3)_2O$, and $C_3H_5(OCOCH_3)OCH_3$, respectively.

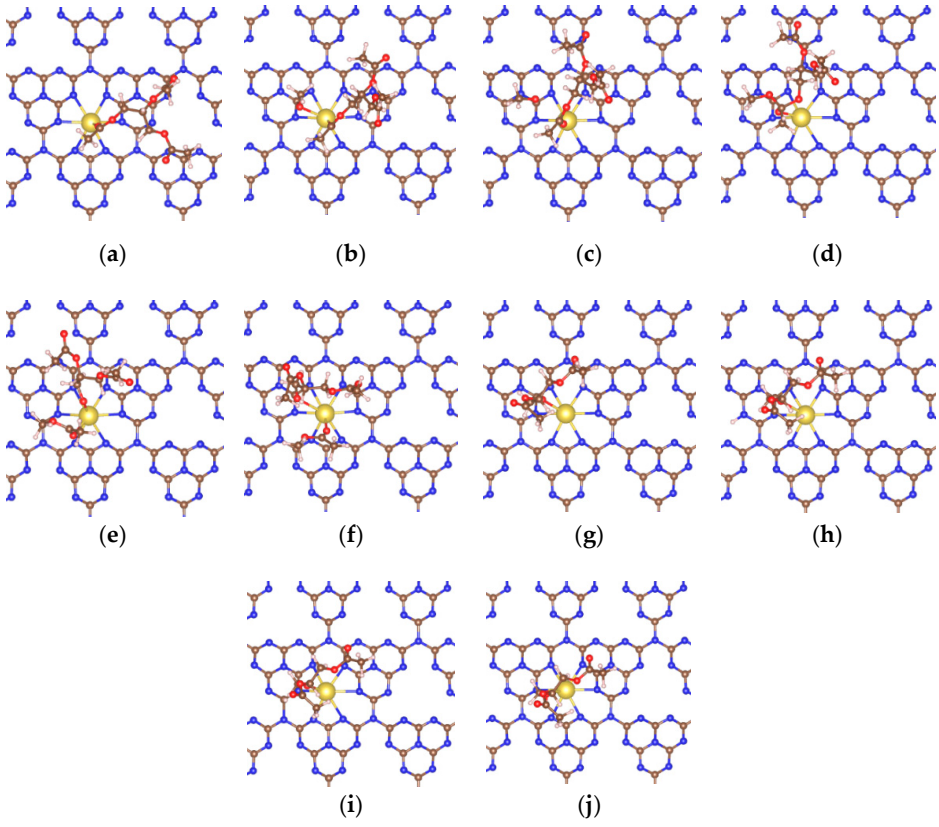

Figure 10. The structure of (**a**) TA*, (**b**) TA* + CH_3O*, (**c**) TS2, (**d**) TA-CH_3O*, (**e**) TS3, (**f**) AAME* + DAO*, (**g**) DAO*, (**h**) DAO* + H*, (**i**) TS4, and (**j**) DAOH* on Na-doped g-C_3N_4, respectively. Blue, brown, yellow, white, and red balls indicate nitrogen, carbon, sodium, hydrogen, and oxygen, respectively.

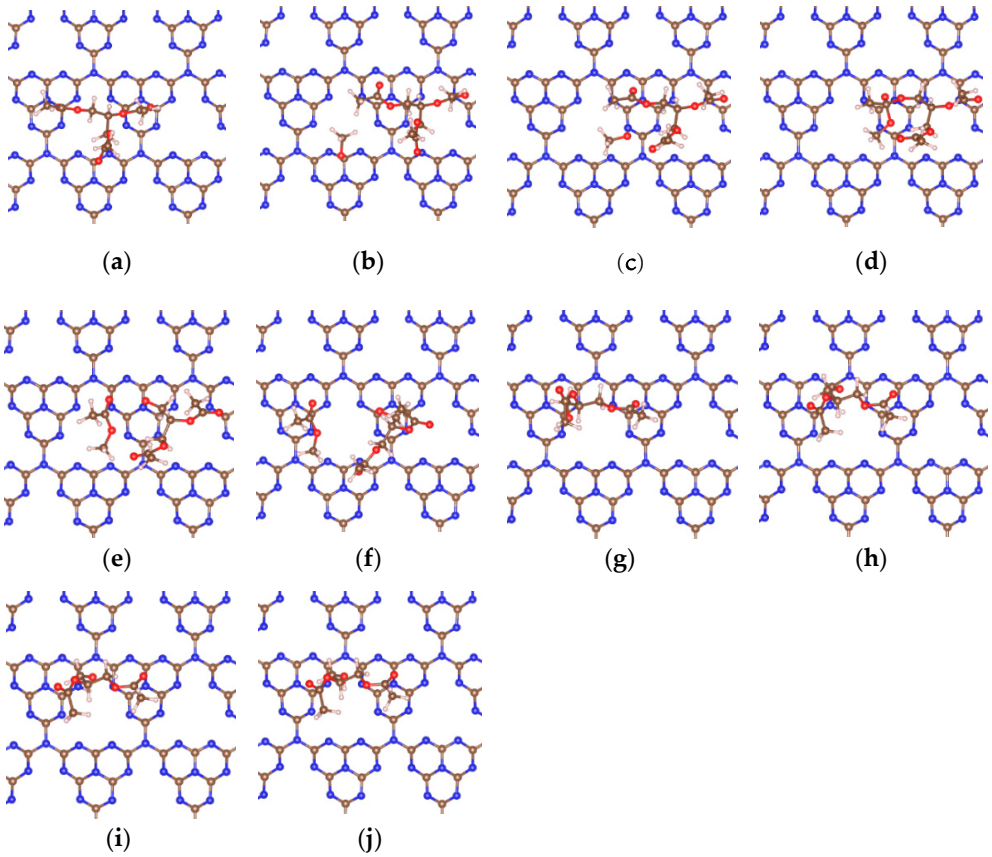

Figure 11. The structure of (**a**) TA*, (**b**) TA* + CH_3O*, (**c**) TS2, (**d**) TA-CH_3O*, (**e**) TS3, (**f**) AAME* + DAO*, (**g**) DAO*, (**h**) DAO* + H*, (**i**) TS4, (**j**) DAOH* on pristine g-C_3N_4, respectively. Blue, brown, yellow, white, and red balls indicate nitrogen, carbon, sodium, hydrogen, and oxygen, respectively.

Table 4. Calculated reaction energy (E_r) of each step in the transesterification of triacetin with CH_3OH. Barrier (E_{barr}) is also shown in parenthesis. Symbol (−)* means the non-activated process (barrier-less). Unit is given in eV.

	Reaction Steps	Pristine	Na-Doped
(1)	CH_3OH (g) → CH_3OH*	−5.30 (−)*	−5.23 (−)*
(2)	CH_3OH* → CH_3O* + H*	−3.17 (1.69)	−4.29 (1.53)
(3)	$C_3H_5(OCOCH_3)_3$ (g) → $C_3H_5(OCOCH_3)_3$*	−5.30 (−)*	−5.39 (−)*
(4)	CH_3O* + $C_3H_5(OCOCH_3)_3$* → $C_3H_5(OCOCH_3)_3OCH_3$*	0.41 (0.41)	−0.47 (0.94)
(5)	$C_3H_5(OCOCH_3)_3OCH_3$* → CH_3COOCH_3* + $C_3H_5(OCOCH_3)_2O$*	−5.26 (−)*	−5.21 (0.43)
(6)	CH_3COOCH_3* → CH_3COOCH_3 (g)	0.19 (−)*	0.29 (−)*
(7)	$C_3H_5(OCOCH_3)_2O$* + H* → $C_3H_5(OCOCH_3)_2OH$*	0.09 (1.65)	−0.43 (1.45)

4. Discussion

In the above sections, we showed the kinetics for the biodiesel (AAME) formation by the reaction of TA (triacetin) with CH_3OH on the heterogeneous Na-doped and pristine

g-C_3N_4 catalysts. By comparing the barriers in each reaction step, we could identify the rate-limiting reaction for the AAME production. That is, we saw that the first CH_3OH decomposition step limited the overall reaction in the Na-doped and pristine catalysts. Note the highest barriers of the (2) $CH_3OH^* \rightarrow CH_3O^* + H^*$ reaction [E_{barr} = 1.53 eV (Na), 1.69 eV (pristine)] compared to other steps [E_{barr} = 0.94 eV (Na), 0.47 eV (pristine) for the (4) $CH_3O^* + C_3H_5(OCOCH_3)_3^* \rightarrow C_3H_5(OCOCH_3)_3OCH_3^*$ step, E_{barr} = 0.43 eV (Na), 0.00 eV (pristine) for the (5) $C_3H_5(OCOCH_3)_3OCH_3^* \rightarrow CH_3COOCH_3^* + C_3H_5(OCOCH_3)_2O^*$ step, E_{barr} = 0.29 eV (Na), 0.18 eV (pristine) for the (7) $C_3H_5(OCOCH_3)_2O^* + H^* \rightarrow C_3H_5(OCOCH_3)_2OH^*$ step]. This indicates a reduced barrier of the Na-doped g-C_3N_4 by 0.16 eV compared to the pristine case in the rate-limiting reaction and, in turn, the enhancement of the transesterification reaction of triacetin toward biodiesel production (AAME).

5. Conclusions

In this study, we examined the role of a single Na atom in enhancing the biodiesel (acetic acid methyl ester) production via the transesterification of triacetin in the Na-doped g-C_3N_4 catalyst by using the density functional theory (DFT) calculation. First, we investigated the acidic and basic properties of Na-doped and pristine g-C_3N_4 by calculating the adsorption energies of NH_3/CO_2 and electronic structure (such as the charge distribution, density of state) of the catalyst. We found that the Na site had a slightly higher Lewis acidity (lower NH_3 adsorption energy) than the pristine case, while the Lewis basicity (CO_2 adsorption energy) was decreased. This was related to the positive characteristics of the Na atom induced by the electron loss of the Na and C (nearby Na) atom to neighboring N atoms. Second, we systematically examined the reaction mechanism of the transesterification of triacetin toward biodiesel (acetic acid methyl ester) production by calculating the reaction energy and barrier of each step. Our DFT calculation showed that the CH_3OH dissociation into CH_3O and H can limit the whole biodiesel production and the addition of a single Na atom into the g-C_3N_4 catalyst substantially reduced the barrier of such rate-limiting step. This indicates that Na-doped g-C_3N_4 is more active than pristine g-C_3N_4 for biodiesel production. This study provides insight into how a single atom dopant modifies the activity of the g-C_3N_4 catalyst toward the transesterification reaction and, in turn, biodiesel production.

Author Contributions: Conceptualization, investigation, and writing, A.C.A., E.K. and H.C.H.; funding acquisition, H.C.H.; supervision, H.C.H., D.-K.K. and H.J.K. All authors have read and agreed to the published version of the manuscript.

Funding: This work was conducted under the framework of the research and development program of the Korea Institute of Energy Research (C2-2431).

Data Availability Statement: Not applicable.

Conflicts of Interest: The authors declare no conflict of interest.

References

1. Xie, W.; Wan, F. Basic ionic liquid functionalized magnetically responsive Fe_3O_4@ HKUST-1 composites used for biodiesel production. *Fuel* **2018**, *220*, 248–256. [CrossRef]
2. Xie, W.; Han, Y.; Wang, H. Magnetic Fe_3O_4/MCM-41 composite-supported sodium silicate as heterogeneous catalysts for biodiesel production. *Renew. Energy* **2018**, *125*, 675–681. [CrossRef]
3. Xie, W.; Fan, M. Biodiesel production by transesterification using tetraalkylammonium hydroxides immobilized onto SBA-15 as a solid catalyst. *Chem. Eng. J.* **2014**, *239*, 60–67. [CrossRef]
4. Sharma, Y.; Singh, B.; Upadhyay, S. Advancements in development and characterization of biodiesel: A review. *Fuel* **2008**, *87*, 2355–2373. [CrossRef]
5. Feyzi, M.; Hassankhani, A.; Rafiee, H.R. Preparation and characterization of Cs/Al/Fe_3O_4 nanocatalysts for biodiesel production. *Energy Convers. Manag.* **2013**, *71*, 62–68. [CrossRef]
6. Xie, W.; Wang, H.; Li, H. Silica-supported tin oxides as heterogeneous acid catalysts for transesterification of soybean oil with methanol. *Ind. Eng. Chem. Res.* **2012**, *51*, 225–231. [CrossRef]

7. Marinković, D.M.; Avramović, J.M.; Stanković, M.V.; Stamenković, O.S.; Jovanović, D.M.; Veljković, V.B. Synthesis and characterization of spherically-shaped CaO/γ-Al2O3 catalyst and its application in biodiesel production. *Energy Convers. Manag.* **2017**, *144*, 399–413. [CrossRef]
8. de Medeiros, T.V.; Macina, A.; Naccache, R. Graphitic carbon nitrides: Efficient heterogeneous catalysts for biodiesel production. *Nano Energy* **2020**, *78*, 105306. [CrossRef]
9. Takase, M.; Zhang, M.; Feng, W.; Chen, Y.; Zhao, T.; Cobbina, S.J.; Yang, L.; Wu, X. Application of zirconia modified with KOH as heterogeneous solid base catalyst to new non-edible oil for biodiesel. *Energy Convers. Manag.* **2014**, *80*, 117–125. [CrossRef]
10. Kaur, N.; Ali, A. Kinetics and reusability of Zr/CaO as heterogeneous catalyst for the ethanolysis and methanolysis of Jatropha crucas oil. *Fuel Proc. Technol.* **2014**, *119*, 173–184. [CrossRef]
11. Manadee, S.; Sophiphun, O.; Osakoo, N.; Supamathanon, N.; Kidkhunthod, P.; Chanlek, N.; Wittayakun, J.; Prayoonpokarach, S. Identification of potassium phase in catalysts supported on zeolite NaX and performance in transesterification of Jatropha seed oil. *Fuel Proc. Technol.* **2017**, *156*, 62–67. [CrossRef]
12. Xie, W.; Zhao, L. Heterogeneous CaO–MoO_3–SBA-15 catalysts for biodiesel production from soybean oil. *Energy Convers. Manag.* **2014**, *79*, 34–42. [CrossRef]
13. Vahid, B.R.; Haghighi, M. Urea-nitrate combustion synthesis of MgO/$MgAl_2O_4$ nanocatalyst used in biodiesel production from sunflower oil: Influence of fuel ratio on catalytic properties and performance. *Energy Convers. Manag.* **2016**, *126*, 362–372. [CrossRef]
14. Rashtizadeh, E.; Farzaneh, F.; Talebpour, Z. Synthesis and characterization of Sr3Al2O6 nanocomposite as catalyst for biodiesel production. *Bioresour. Technol.* **2014**, *154*, 32–37. [CrossRef] [PubMed]
15. Xie, W.; Zhao, L. Production of biodiesel by transesterification of soybean oil using calcium supported tin oxides as heterogeneous catalysts. *Energy Convers. Manag.* **2013**, *76*, 55–62. [CrossRef]
16. Saeedi, M.; Fazaeli, R.; Aliyan, H. Nanostructured sodium–zeolite imidazolate framework (ZIF-8) doped with potassium by sol–gel processing for biodiesel production from soybean oil. *J. Sol. Gel. Sci. Technol.* **2016**, *77*, 404–415. [CrossRef]
17. Xie, W.; Han, Y.; Tai, S. Biodiesel production using biguanide-functionalized hydroxyapatite-encapsulated-γ-Fe_2O_3 nanoparticles. *Fuel* **2017**, *210*, 83–90. [CrossRef]
18. Raita, M.; Arnthong, J.; Champreda, V.; Laosiripojana, N. Modification of magnetic nanoparticle lipase designs for biodiesel production from palm oil. *Fuel Proc. Technol.* **2015**, *134*, 189–197. [CrossRef]
19. Liu, Y.; Zhang, P.; Fan, M.; Jiang, P. Biodiesel production from soybean oil catalyzed by magnetic nanoparticle $MgFe_2O_4$@ CaO. *Fuel* **2016**, *164*, 314–321. [CrossRef]
20. Wu, Z.; Li, Z.; Wu, G.; Wang, L.; Lu, S.; Wang, L.; Wan, H.; Guan, G. Brønsted acidic ionic liquid modified magnetic nanoparticle: An efficient and green catalyst for biodiesel production. *Ind. Eng. Chem. Res.* **2014**, *53*, 3040–3046. [CrossRef]
21. Xie, W.; Zang, X. Immobilized lipase on core–shell structured Fe_3O_4–MCM-41 nanocomposites as a magnetically recyclable biocatalyst for interesterification of soybean oil and lard. *Food Chem.* **2016**, *194*, 1283–1292. [CrossRef] [PubMed]
22. Masih, D.; Ma, Y.; Rohani, S. Graphitic C_3N_4 based noble-metal-free photocatalyst systems: A review. *Appl. Catal. B Environ.* **2017**, *206*, 556–588. [CrossRef]
23. Thomas, A.; Fischer, A.; Goettmann, F.; Antonietti, M.; Müller, J.-O.; Schlögl, R.; Carlsson, J.M. Graphitic carbon nitride materials: Variation of structure and morphology and their use as metal-free catalysts. *J. Mater. Chem* **2008**, *18*, 4893–4908. [CrossRef]
24. Goglio, G.; Foy, D.; Demazeau, G. State of Art and recent trends in bulk carbon nitrides synthesis. *Mater. Sci. Eng. R Rep.* **2008**, *58*, 195–227. [CrossRef]
25. Nasir, M.S.; Yang, G.; Ayub, I.; Wang, S.; Wang, L.; Wang, X.; Yan, W.; Peng, S.; Ramakarishna, S. Recent development in graphitic carbon nitride based photocatalysis for hydrogen generation. *Appl. Catal. B Environ.* **2019**, *257*, 117855. [CrossRef]
26. Luo, B.; Song, R.; Jing, D. Significantly enhanced photocatalytic hydrogen generation over graphitic carbon nitride with carefully modified intralayer structures. *Chem. Eng. J.* **2018**, *332*, 499–507. [CrossRef]
27. Ismael, M.; Wu, Y.; Taffa, D.H.; Bottke, P.; Wark, M. Graphitic carbon nitride synthesized by simple pyrolysis: Role of precursor in photocatalytic hydrogen production. *New J. Chem.* **2019**, *43*, 6909–6920. [CrossRef]
28. Shen, M.; Zhang, L.; Shi, J. Converting CO_2 into fuels by graphitic carbon nitride-based photocatalysts. *Nanotechnology* **2018**, *29*, 412001. [CrossRef]
29. Huang, P.; Huang, J.; Pantovich, S.A.; Carl, A.D.; Fenton, T.G.; Caputo, C.A.; Grimm, R.L.; Frenkel, A.I.; Li, G. Selective CO_2 reduction catalyzed by single cobalt sites on carbon nitride under visible-light irradiation. *J. Am. Chem. Soc.* **2018**, *140*, 16042–16047. [CrossRef]
30. Shen, M.; Zhang, L.; Wang, M.; Tian, J.; Jin, X.; Guo, L.; Wang, L.; Shi, J. Carbon-vacancy modified graphitic carbon nitride: Enhanced CO_2 photocatalytic reduction performance and mechanism probing. *J. Mater. Chem. A* **2019**, *7*, 1556–1563. [CrossRef]
31. Roy, S.; Reisner, E. Visible-Light-Driven CO_2 Reduction by Mesoporous Carbon Nitride Modified with Polymeric Cobalt Phthalocyanine. *Angew. Chem. Int. Ed.* **2019**, *58*, 12180–12184. [CrossRef] [PubMed]
32. Wen, J.; Xie, J.; Chen, X.; Li, X. A review on g-C3N4-based photocatalysts. *Appl. Surf. Sci.* **2017**, *391*, 72–123. [CrossRef]
33. Wang, A.; Wang, C.; Fu, L.; Wong-Ng, W.; Lan, Y. Recent advances of graphitic carbon nitride-based structures and applications in catalyst, sensing, imaging, and LEDs. *Nano Micro Lett.* **2017**, *9*, 1–21. [CrossRef] [PubMed]
34. Hohenberg, P.; Kohn, W. Inhomogeneous electron gas. *Phys. Rev.* **1964**, *136*, B864. [CrossRef]

35. Kresse, G.; Furthmüller, J. Efficient iterative schemes for ab initio total-energy calculations using a plane-wave basis set. *Phys. Rev. B* **1996**, *54*, 11169. [CrossRef] [PubMed]
36. Blöchl, P.E. Projector augmented-wave method. *Phys. Rev. B* **1994**, *50*, 17953. [CrossRef]
37. Perdew, J.P.; Burke, K.; Ernzerhof, M. Generalized gradient approximation made simple. *Phys. Rev. Lett.* **1996**, *77*, 3865. [CrossRef]
38. Weinan, E.; Ren, W.; Vanden-Eijnden, E. String method for the study of rare events. *Phys. Rev. B* **2002**, *66*, 052301.
39. Weinan, E.; Ren, W.; Vanden-Eijnden, E. Simplified and improved string method for computing the minimum energy paths in barrier-crossing events. *J. Chem. Phys.* **2007**, *126*, 164103.
40. Henkelman, G.; Uberuaga, B.P.; Jónsson, H. A climbing image nudged elastic band method for finding saddle points and minimum energy paths. *J. Chem. Phys.* **2000**, *113*, 9901–9904. [CrossRef]
41. Tang, W.; Sanville, E.; Henkelman, G. A grid-based Bader analysis algorithm without lattice bias. *J. Phys. Condens. Matter* **2009**, *21*, 084204. [CrossRef] [PubMed]
42. Arellano, J.; Molina, L.; Rubio, A.; Alonso, J. Density functional study of adsorption of molecular hydrogen on graphene layers. *J. Chem. Phys.* **2000**, *112*, 8114–8119. [CrossRef]
43. Momma, K.; Izumi, F. VESTA 3 for three-dimensional visualization of crystal, volumetric and morphology data. *J. Appl. Crystallogr.* **2011**, *44*, 1272–1276. [CrossRef]
44. Wu, S.; Yu, Y.; Qiao, K.; Meng, J.; Jiang, N.; Wang, J. A simple synthesis route of sodium-doped g-C_3N_4 nanotubes with enhanced photocatalytic performance. *J. Photochem. Photobiol. A Chem.* **2021**, *406*, 112999. [CrossRef]
45. Rajput, J.K. Alkali metal (Na/K) doped graphitic carbon nitride (g-C_3N_4) for highly selective and sensitive electrochemical sensing of nitrite in water and food samples. *J. Electroanal. Chem.* **2020**, *878*, 114605.
46. Zhu, S.; Cao, X.; Cao, X.; Feng, Y.; Lin, X.; Han, K.; Li, X.; Deng, P. Metal-doped (Fe, Nd, Ce, Zr, U) graphitic carbon nitride catalysts enhance thermal decomposition of ammonium perchlorate-based molecular perovskite. *Mater. Des.* **2021**, *199*, 109426. [CrossRef]
47. Zhu, B.; Zhang, L.; Cheng, B.; Yu, J. First-principle calculation study of tri-s-triazine-based g-C_3N_4: A review. *Appl. Catal. B Environ.* **2018**, *224*, 983–999. [CrossRef]
48. Sharma, S.; Saxena, V.; Baranwal, A.; Chandra, P.; Pandey, L.M. Engineered nanoporous materials mediated heterogeneous catalysts and their implications in biodiesel production. *Mater. Sci. Energy Technol.* **2018**, *1*, 11–21. [CrossRef]
49. Gorji, A.; Ghanei, R. A review on catalytic biodiesel production. *J. Biodivers. Environ. Sci.* **2014**, *5*, 48–59.